

Photometric redshift using the far-infrared SED

T. Wiklind

*European Space Agency Space Telescope Division
Space Telescope Science Institute
3700 San Martin Dr., Baltimore MD 21218, USA*

wiklind@stsci.edu

ABSTRACT

A method for using the sub-millimeter band to determine photometric redshifts of luminous high- z dusty galaxies is presented. It is based on the observation that local ultra-luminous IR galaxies show an average spectral energy distribution which has a remarkably small dispersion for wavelengths $\lambda > 50\mu\text{m}$. The shape of the long wavelength part is independent on whether the local ULIRG possesses an AGN or not. A local template is derived from a sample of ULIRG data presented by Klaas et al. (2001). Using this template and the internal dispersion in its shape, it is shown that observations at two fixed submm wavelengths, e.g. $450\mu\text{m}$ and $850\mu\text{m}$, can be used to determine the photometric redshift of galaxies in the redshift range $1 < z < 5$. The uncertainty in the redshift arising from the template SED amounts to $\Delta z/z \sim 0.3$, with an improvement at the higher redshift range. Implications for using this method together with the large instantaneous bandwidth of the Atacama Large Millimeter Array (ALMA) for deriving spectroscopic redshifts using CO emission is discussed.

Subject headings: techniques: photometric, galaxies: distances and redshifts, galaxies: high redshift, galaxies: photometry, submillimeter

1. Introduction

The spectral shape of the far-infrared background suggests that as much as half of the energy ever emitted by stars and AGNs has been absorbed by dust grains and re-radiated in the far-infrared (Puget et al. 1996; Fixsen et al. 1998; Gispert, Lagache & Puget 2000). Recent observations at sub-millimeter wavelengths have revealed a population of objects believed to be dusty high redshift far-infrared luminous galaxies (Smail et al. 1997; Barger et al. 1998; Hughes et al. 1998; Eales et al. 1999). These sources emit most of their bolometric

luminosity in the far-infrared (FIR), and are believed to account for a large portion of the far-infrared background (e.g. Blain 1999). Although detailed redshift information is still lacking for most of these sources, they are believed to be situated at $z > 1$. Number-counts then indicate a large excess of sources compared to no-evolution models based on optical surveys (Guiderdoni et al. 1998; Blain 1999; Scott et al. 2002b), suggesting that the optically derived star formation density is significantly underestimated at high redshifts. This strong evolution is difficult to reproduce in semi-analytical hierarchical Cold Dark Matter models (Devriendt & Guiderdoni 2000; Kaviani, Haehnelt & Kauffmann 2002). Assuming similar dust and FIR properties between the high- and low- z objects, the CDM models under-estimate the observed number counts by almost two orders of magnitude (Kaviani et al. 2002).

A remaining and central uncertainty in the discussion about the properties of the dusty high redshift population is their actual redshift distribution. Despite detection of >100 sub-millimeter sources, only a handful have secure optical or near-infrared counterparts (cf. Smail et al. 2002). This lack of counterparts shows that the submm sources are very faint ($R \geq 25$ and $K \geq 21$), making it difficult to obtain redshifts even with 8-10m class telescopes, should the counterparts be identified. The presence of large amounts of dust also makes optical/NIR photometric redshift determinations unreliable, should the continuum be detected.

Ultra-deep long wavelength radio continuum surveys have shown that many of the submm detected objects are related to weak radio sources (Smail et al. 2000). Chapman et al. (2002b) find that $\sim 2/3$ of sources detected at $850\mu\text{m}$ are also radio-identified at sub-mJy levels. For local galaxies there exists a very tight correlation between the long wavelength radio continuum and the far-infrared at $60\mu\text{m}$ and $100\mu\text{m}$, extending over almost four orders of magnitude in luminosity (Condon 1992). The physical mechanism for this correlation is believed to be the formation of massive stars, which heats the dust through their UV radiation, producing the FIR emission, and supernova explosions producing relativistic electrons which give synchrotron emission in the radio regime. Based on this tight correlation between non-thermal radio and thermal far-infrared fluxes for local galaxies, Carilli & Yun (1999) devised a technique to use the radio-FIR spectral index as a redshift indicator for distant submm sources. The technique uses the fact that for a fixed observed wavelength, the flux of synchrotron emission decreases with increasing redshift, while the opposite is true for the Rayleigh-Jeans part of the dust continuum. The first implementation used two local starburst galaxies as templates (see also Barger et al. 1998). A follow-up study (Carilli & Yun 2000) used 17 low- z star-forming galaxies as templates. The result is a submm-radio spectral index which depends on the redshift of the source.

There are several caveats with this radio-FIR relation. The spectral index depends not only on the redshift of the source, but also on several other parameters, most notably the dust

temperature, and the radio continuum spectral index, for instance non-thermal vs. thermal contributions and the possible presence of an AGN. The decrease of the observed radio continuum with increasing redshift makes it increasingly demanding to detect the sources as z increases. The radio-FIR relation is therefore practical up to $z \sim 2$. Dunne et al. (2001) discuss the various dependencies, comparing with a local sample of FIR bright galaxies. Nevertheless, although the radio-FIR technique is too crude to be used as a photometric redshift indicator for individual sources, becomes unreliable at $z > 2$, and care has to be exercised in order not to include radio-loud AGNs, it has proven that the submm detected sources, seen as a class, are indeed situated at high redshifts. Very little is known about these sources from other wavelength bands, therefore this information has been crucial for establishing the presence of a high redshift population of dusty, luminous and, in the few known cases, massive galaxies.

Several authors have speculated on the possibility of using two or more wavelength bands in the sub-millimeter as a mean of deriving photometric redshifts (e.g. Hughes et al. 1998; Blain 1999; Blain, Barnard & Chapman 2002). The conclusion has been that this is unfeasable due to a degeneracy between the redshift and dust temperature (see Sect. 2.3). In a recent study by Hughes et al. (2002) the submm photometric method is revived using local starburst galaxies and a statistical treatment.

In this paper an alternative method for determining the redshift of submm detected sources is presented, using only the Rayleigh-Jeans part of the dust SED. It is based on the existence of a template SED for local ULIRGs, which shows a remarkably uniform shape at wavelengths $60\mu\text{m} < \lambda < 1250\mu\text{m}$. Assuming that ultraluminous IR galaxies at high redshift have similar properties, the flux ratio of two submm bands, for instance at $850\mu\text{m}$ and $450\mu\text{m}$, is thus sensitive to the redshift of the source in the range $1 < z < 5$. A comparison with submm flux ratios for a sample of high- z AGNs (mostly gravitationally lensed) shows that this technique is accurate enough to allow a redshift determination to within $\sim 30\%$. With the advent of new submm telescopes and instruments, such as APEX (Atacama Pathfinder EXperiment), ALMA (Atacama Large Millimeter Array) and SCUBA II, some of them capable of operating up to $325\mu\text{m}$, the use of submm flux ratios is foreseen to become a technique to quickly estimate approximate redshifts of large numbers of submm detected sources.

2. Dust Spectral Energy Distributions

In this section I will briefly discuss dust spectral energy distributions and how these can be used to describe physical properties of unresolved dust sources observed in the IR-

to-submm. The main conclusion is that extreme care has to be exercised when doing this interpretation since it can easily lead to wrong inferences about dust mass and the physical size of the emitting region.

2.1. Models

The far-infrared spectral energy distribution of dust emission is purely thermal and usually represented by a modified blackbody curve, $S_\nu \propto \nu^\beta B_\nu(T_d)$, where B_ν is the Planck function, T_d the dust temperature and ν^β is the grain emissivity power-law index. The index is in the range $\beta = 1 - 2$. A single-size and uniform grain composition would lead to $\beta = 1$. When $\beta > 1$ it is indicative of a distribution of grain sizes and/or compositions. Such simple representation has successfully been used for cold dust components where a large part of the SED is optically thin. When $\tau \approx 1$ or larger, the observed dust emission needs to be described by an expression of the form:

$$S_\nu = \Omega_s B_\nu(T_d) (1 - e^{-\tau_\nu}) , \quad (1)$$

where Ω_s is the solid angle of the source emissivity distribution and τ_ν is the opacity of the dust. Setting $\tau_\nu = (\nu/\nu_0)^\beta$ gives $S_\nu \propto \nu^\beta B_\nu(T_d)$ for $\tau_\nu \ll 1$ and $S_\nu \propto B_\nu(T_d)$ for $\tau_\nu \gg 1$. The critical frequency ν_0 is the frequency where $\tau_\nu = 1$. The FIR luminosity is obtained by integrating Eq. 1 over all frequencies:

$$L_{\text{IR}} = 4\pi (1+z)^3 D_A^2 \int_0^\infty S_\nu d\nu , \quad (2)$$

where D_A is the angular size distance¹ With the substitution $x = h\nu/kT$, we can express Eq. 2 in a form directly accessible for integration (e.g. Wiklind & Alloin 2003):

$$\frac{L_{\text{IR}}}{L_\odot} = 8.53 \times 10^{10} (1+z)^3 D_A^2 T_d^4 \Omega_s \int_0^\infty \frac{x^3 (1 - e^{-(ax)^\beta})}{e^x - 1} dx , \quad (3)$$

The integral can be evaluated numerically with appropriate values of the parameter $a = kT_d/h\nu_0$. The solid angle Ω_s is a parameter derived in the fitting procedure. In the event of a single dust component and a source unresolved by the telescope, Ω_s can be estimated from the measured flux S_{ν_r} at a given restframe frequency ν_r .

$$\Omega_s = \frac{S_{\nu_r}}{B_{\nu_r}(T_d) (1 - e^{-(\nu_r/\nu_0)^\beta})}$$

¹Unless otherwise stated, all distances will be expressed in Mpc, frequencies in GHz and fluxes in Jansky.

$$\approx 6.782 \times 10^{-4} \nu_r^{-3} S_{\nu_r} \left[\frac{e^{h\nu_r/kT_d} - 1}{1 - e^{-(\nu_r/\nu_0)^\beta}} \right]. \quad (4)$$

A rough estimate of the equivalent spherical radius of the emitting region can be obtained from Ω_s ; $r \approx D_A \sqrt{\Omega_s/\pi}$.

An estimate of the dust mass from the infrared flux requires either optically thin emission combined with a knowledge of the grain properties, or optically thick emission and a knowledge of the geometry of the emission region (cf. Hildebrand 1983). The grain properties are characterized through the macroscopic mass absorption coefficient, κ_ν (cf. Hughes, Dunlop & Rawlins 1997). Combining several estimates (cf, Hildebrand 1983; Hughes et al. 1997), the mass absorption coefficient can be described as:

$$\kappa_{\nu_r} \approx 0.15 \left(\frac{\nu_r}{375 \text{ GHz}} \right)^{1.5} \text{ m}^2 \text{ kg}^{-1}. \quad (5)$$

This expression corresponds to a grain composition similar to that found in the Milky Way. At frequencies where the emission is optically thin, the dust mass can now be determined from

$$M_d = \frac{S_{\nu_{obs}}}{\kappa_{\nu_r} B_{\nu_r}(T_d)} D_A^2 (1+z)^3, \quad (6)$$

which can be expressed as:

$$M_d \approx 4.08 \times 10^4 S_{\nu_{obs}} D_A^2 \left(\frac{\nu_r}{375 \text{ GHz}} \right)^{-9/2} \left(e^{h\nu_r/kT_d} - 1 \right) (1+z)^3 M_\odot. \quad (7)$$

2.2. Multiple components

In reality, it is likely that a galaxy contains several different dust components each characterized by a different set of parameters. Lacking observational data with sufficient spatial resolution, it is usually assumed that the dust emission can be decomposed into three main components (e.g. Rowan-Robinson 1986, 1992); cool dust associated with a cirrus component heated by the diffuse interstellar radiation field, warm dust associated with regions of massive star formation, and, if the galaxy harbors an AGN, a hot component representing dust heated by the central AGN. These three dust components will dominate the submm, FIR and mid-IR wavelength regimes, respectively. There are, however, no assumptions about their actual sizes or their geometries.

More elaborate models solve the radiation of transfer in a dusty medium containing heating sources (e.g. Granato, Danese & Franceschini 1996; Efstathiou, Rowan-Robinson &

Siebenmorgen 2000). Due to the large number of parameters, involving dust variables as a function of the geometry, these methods can only be safely applied to sources and parts of the SED which are known to be associated with a single heating source, e.g. an AGN.

The representation of the dust SED discussed in Sect. 2.1 involves four parameters per component. Since most observed SEDs contain only a few data points, a fit of Eq. 1 is prone to a relatively large degree of freedom, especially if more than one dust component is used. Moreover, at long wavelengths there exists a degeneracy between the dust temperature T_d and the grain emissivity power-law index β (e.g. Blain et al. 2002). This degeneracy is difficult to resolve without an observationally well sampled SED.

Due to the observationally sparsely sampled dust SEDs, the dust emission is often characterized by fitting a single component. This usually gives a reasonable fit to the observed data points, but should not be over-interpreted in terms of physical conditions of the dust grains or of global dust parameters, especially dust mass. This is illustrated in Fig. 1 where the dust SED of the local ULIRG 17208-0014 has been fitted using both one and two dust component SEDs of the type described above (see also Klaas et al. 2001). The single component SED is characterized by a dust temperature of 59 K and an exponent $\beta = 1.8$. The two component SED has warm dust grains characterized by a temperature of 53 K and $\beta = 1.6$, and a cool component with $T_d = 27$ K and $\beta = 2.0$. While the two component SED has critical frequencies ν_0 corresponding to $35\mu\text{m}$ and $51\mu\text{m}$, respectively, the single component SED becomes optically thick already at $214\mu\text{m}$. Both models give approximately the same L_{FIR} , showing that they describe the *shape* of the SED reasonably well. The single component SED, however, gives a total dust mass which is 3.5 times smaller than the two-component SED. This is due to the highly non-linear relation between $M_{\text{dust}}/L_{\text{FIR}}$ as a function of dust temperature; while $M_d \propto \exp(h\nu_r/kT_d)$, (approximately $\propto T_d^{-1}$ at long wavelengths), the luminosity $L_{\text{FIR}} \propto T_d^{4-5}$. It is thus possible to ‘hide’ a large amount of dust in a low temperature component. In terms of typical size scales, the cool dust extends over an area which is ~ 150 times larger than the warm component.

Although the resulting χ^2 values for the fits shown in Fig. 1 are similar, they describe dust components with widely different physical properties. The two fits, however, both give a satisfactory description of the overall *shape* of the SED. This is important to keep in mind when discussing and comparing dust properties of different types of objects, and, as argued here, when constructing a template SED.

2.3. Degeneracy between T_d and redshift

Lowering the temperature of a modified blackbody curve is equivalent to shifting the entire spectrum towards longer wavelengths. A similar shift can be achieved by keeping the temperature constant but moving the source to a larger redshift. Hence, without knowing the dust temperature a priori, it is impossible to distinguish between a source at large redshift with a given T_d and a source at low redshift with a dust SED characterized by a lower temperature (e.g. Blain 1999; Eales et al. 1999; Blain, Barnard & Chapman 2002).

In order to use two flux densities at the FIR/submm part of a dust SED to determine a photometric redshift of the source, it is thus necessary to know the shape of the SED in sufficient detail. This can be done if the global physical parameters for the emission can be established. If this is not the case, the degeneracy between the dust temperature and redshift makes progress essentially impossible.

The effect of this degeneracy is illustrated in Fig. 2 for a simple dust SED. The ratio of flux densities at $325\mu\text{m}$ and $850\mu\text{m}$ of a single component modified blackbody function (given by Eq 1) are plotted as a function of redshift. The result for six different dust temperatures between 30 K and 80 K are shown. Despite the fact that the gradient of the flux ratio as a function of redshift is quite steep, the effect of the dust temperature precludes its use as a redshift indicator unless T_d is known.

Attempts to characterize local FIR luminous galaxies in terms of dust parameters show a relatively broad range in T_d and β (e.g. Sanders & Mirabel 1996; Klaas et al. 2001). As shown above, a sparsely sampled dust SED can be equally well modeled with one and two component dust SEDs, with different sets of dust parameters, leading to an even larger spread in parameter values for different sources. Similarly good fits can also be achieved for different dust temperatures by varying the index β . The *shape*, however, remains basically identical and the ratio of FIR/submm flux densities are approximately the same for the various fits.

3. Photometric Redshift

3.1. The local template

Local ULIRGs are characterized by a dominating FIR luminosity, $L_{\text{FIR}} \geq 10^{12} L_{\odot}$, large dust masses, large molecular gas masses and signs of strong gravitational interaction and/or merging (e.g. Sanders & Mirabel 1996; Rigopoulou et al. 1999). In addition, the dust and gas is strongly concentrated to the central regions of the galaxies (Downes & Solomon 1998).

The heating source of the large FIR luminosity is in many cases pure star formation, but a significant fraction of all ULIRGs also contain an AGN (Rigopoulou et al. 1999; Klaas et al. 2001). Local ULIRGs have properties which in many respects are similar to those of the submm detected population, especially those few that have known redshift and have been studied in greater detail (cf. Ivison 2000). Two submm detected galaxies are known to contain large amount of molecular gas as seen through their CO emission (Fruyer et al. 1998, 1999). Using the standard conversion ratio between CO and molecular hydrogen, H_2 , the gas masses are in the range $(0.5 - 2.0) \times 10^{11} M_\odot$, showing that these objects are indeed as massive and gas-rich as local ULIRGs. Local ULIRGs are therefore the most likely low- z counterparts to the high redshift dusty submm objects.

A recent compilation of NIR-to-submm observations of 41 local ultraluminous infrared galaxies was presented in Klaas et al. (2001). The sample consists of galaxies with $L_{\text{FIR}} > 10^{12} L_\odot$, with most objects having redshift $z \leq 0.1$. The observational data was obtained with several different instruments. The NIR bands (1.2 and $2.2\mu\text{m}$) was observed using the 2.2m Calar Alto telescope. The IR data between 10-200 μm was obtained using the ISO. Sub-millimeter data at 450 μm and 850 μm was obtained for a sub-set of 16 objects using the JCMT. A few millimeter continuum observations were also done with the SEST (Swedish-ESO Submillimeter Telescope). The SEDs represent the most complete set of IR/FIR/submm photometric data obtained for local ULIRGs to date. Given the observed similarities between submm detected sources and the local ULIRGs, the Klaas et al. sample is well suited for creating a ‘template’ SED to be used for the high redshift counterparts.

In October 2002 we observed 8 of the sources in the Klaas et al. (2001) sample using the SIMBA bolometer array at the Swedish-ESO-Submillimeter telescope (SEST) in Chile. The SIMBA instrument is a 37-channel bolometer array operating at 1250 μm (see Nyman et al. 2001 for a description of SIMBA). It uses a fast mapping technique and achieves a sensitivity of $\sim 70 \text{ mJy s}^{-1/2} \text{ pixel}^{-1}$. Four of the local ULIRGs were positively detected. The results are presented in Table 1. The 1250 μm result for the source 17208-0014 is used in Fig. 1, where the long wavelength data implies the presence of a cold dust component. This aspect of the dust continuum will be discussed in a forthcoming paper. The 1250 μm data is not used in the present analysis.

In order to avoid redshift corrections to the local sample, 4 objects from the Klaas et al. (2001) source list, with redshifts in the range $z = 0.2 - 0.3$, were discarded. The remaining 37 objects all have $z \leq 0.1$. The SEDs of these 37 sources, as tabulated by Klaas et al., are plotted in Fig. 3. No corrections or normalization have been done to the SEDs at this stage. It is clear from the figure that although the observed flux densities vary by two orders of magnitude, the general shapes of the SEDs appear quite uniform.

In order to quantify the impression of a uniform shape of the SED, the individual SEDs, S_i where multiplied with a constant A_i chosen such that the overall dispersion is minimized. In the present case, all the wavelengths were given equal weights. No significant change could be found when restricting the wavelengths to the FIR and sub-millimeter. The result is shown in Fig. 4, where the average flux (arbitrary normalization) at each observed wavelength is shown together with the 1σ deviation. In Fig. 4 the resulting individual measurements are also shown. It is clear that the impression of a general shape of the SEDs is correct only for wavelengths $\lambda > 50\mu\text{m}$. At mid-IR wavelengths, the dispersion is considerable. At near-IR wavelengths the dispersion is again smaller than in the mid-IR.

3.2. The method

3.2.1. Fitting a single SED

The small dispersion of the average spectral energy distribution of local ULIRGs at wavelengths longer than $50\mu\text{m}$ (Fig. 4) allows a modified blackbody curve of the type discussed in Sect. 2 to be fitted to the average SED over this interval. Although a two component fit is marginally superior to a single component, especially around $90 - 120\mu\text{m}$, a single component dust SED was used for simplicity. The fitted function is given by Eq. 1 and the uncertainty associated with each observed wavelength is taken to be the dispersion obtained from the the average SED shown in Fig. 4.

A least-square fit of Eq. 1 gives the following parameters: $\Omega = (1.6 \pm 0.6) \times 10^{-13}$, $\beta = 1.8 \pm 0.5$, $\nu_0 = (1.2 \pm 0.4) \times 10^{12}$ Hz ($250\mu\text{m}$) and $T_d = 68 \pm 9$ K. The Ω parameter is necessary for the fit but otherwise arbitrary since the average SED has already been normalized. The χ^2 is 0.89. As emphasized in Sect. 2, the physical reality of the dust properties associated with the fit is debatable. However, the shape of the SED is well described by the fitted parameter.

The resulting fitted SED is shown in Fig. 5 together with the normalized data points. Only data in the wavelength range $60 \leq \lambda \leq 850\mu\text{m}$ were used in the fit. The fitted curve coincides very tightly with all the average data points in the range $25 \leq \lambda \leq 850\mu\text{m}$, but only the $60 - 850\mu\text{m}$ range will be considered in the following. The $1250\mu\text{m}$ data were omitted because of a small number of observations and the possibility of contribution from a very cold dust component. Such a cold component would not be visible when observing at shorter wavelengths and definitely not for sources at high redshifts. The presence of such a cold dust component in at least one of the sources in the present sample is suggested by the excess flux density at $\lambda = 1250\mu\text{m}$ seen in Fig. 1.

3.2.2. Monte Carlo simulation

In order to estimate the uncertainty associated with the fit of the single dust component, given the dispersion of the average SED, a Monte Carlo simulation was done. For 10^4 realizations the average values of the underlying data points were stochastically and uniformly varied within $\pm 1\sigma$. For each simulated data set a least-square fit of Eq. 1 was done. The fits were done using data in the wavelength range $60\mu\text{m} \leq \lambda \leq 850\mu\text{m}$. The resulting SEDs are shown in Fig. 6. All the 10^4 curves are plotted and they define an envelope which remains well constrained in the wavelength range $60 - 850\mu\text{m}$, but which diverges at shorter and longer wavelengths (where the fits are no longer constrained by data). The fit to each of the Monte Carlo realizations were done in the same manner as the fit discussed above.

3.2.3. Flux ratios

The observed flux at a given wavelength band is obtained by multiplying Eq. 1, using the fitted parameters, with a normalized filter response function and then integrating over wavelength and normalizing with the filter response function. Here a simple top-hat function is used, with the same width as the filters used on SCUBA, i.e. 30 GHz for both $450\mu\text{m}$ and $850\mu\text{m}$. The same width was also used for the $325\mu\text{m}$ band². By redshifting the underlying SED and correcting for the $(1+z)$ compression, the flux ratio at a given redshift was calculated.

The flux density ratio at two fixed wavelengths as a function of redshift was obtained for each of the Monte Carlo realizations. They are plotted in Fig. 7 for both $325/850\mu\text{m}$ and $450/850\mu\text{m}$. The grey-scale corresponds to the density of curves passing through a given point in the diagram, the darker the shade the higher the density. The white full drawn line marks the ridge of highest density and it is flanked by two lines marking the boundary containing 95% of the curves on either side of the ridge. By taking a cut at a constant flux ratio, it is possible to assess the formal error in estimated redshift. This error is for the most part non-gaussian. In reality there will be an uncertainty associated with the measured flux ratio as well. The predicted redshift will be enclosed by a box-shaped region, limited by the high end of the flux ratio uncertainty at the lower redshift end and the lower flux ratio uncertainty at the higher redshift end.

²This wavelength was chosen in anticipation of the planned bolometer camera for APEX (Atacama Pathfinder EXperiment). The precise wavelength coverage and the shape of the filter response function are not known presently. The results presented here for this short wavelength band must therefore be recalculated once the filter response is determined.

At redshifts $z \leq 1$, the dispersion in redshift is too large for the flux ratio to contain any predictive power of the redshift. This is due to the fact that at small redshifts, both of the observed wavelengths probe a section of the Rayleigh-Jeans part of the modified blackbody curve with a close to a pure power law form. The flux ratio therefore remains almost constant. The insensitivity to low redshifts is less pronounced for the $325/850\mu\text{m}$ flux ratio since the shorter wavelength will be affected by non-linearities in the dust SED at lower redshifts than the $450\mu\text{m}$ band. At high enough redshifts the shorter wavelength band will reach the Wien side of the modified blackbody curve. The flux ratios will again start to become more or less constant. For the present sample this effect will set in at redshifts $z \geq 5$. The most accurate predictive power for the redshift therefore exists in the redshift range $1 \leq z \leq 5$.

4. Discussion and Conclusion

4.1. Selection effects

Any method of photometric redshift is based on the assumption that we know or can model the spectral energy distribution of high redshift objects. Modeling the FIR/submm SED is difficult due to a degeneracy between the dust temperature and the grain emissivity power-law index β . Moreover, as discussed in Sect. 2.3, lowering the dust temperature of a nearby source gives a similar effect on the SED as moving the source to a higher redshift while keeping the temperature constant. These degeneracies makes it impossible to use the FIR/submm SED for photometric redshift determinations if one do not have a sufficiently good apriori knowledge of the dust properties of the object in question. There appears to exist a relation between the dust temperature and FIR luminosity (e.g. Dunne et al. 2000; Blain et al. 2002), which can possibly be used to break the degeneracy. This Luminosity-Temperature (LT) relation is, however, presently poorly determined.

In Sect. 3.1 it was shown that the SED of local ultraluminous IR galaxies has a remarkably similar shape at wavelengths longer than $\lambda \geq 50\mu\text{m}$. The similarity in the shape of the SEDs could very well be an effect of sample selection. The local galaxies was selected as being ULIRGs, meaning that they have a $L_{\text{FIR}} \geq 10^{12} L_{\odot}$. At the same time, all the sources have $L_{\text{FIR}} < 10^{13} L_{\odot}$. If there exists a LT-relation, this selection of sources within a limited luminosity range favors those which have similar dust temperatures. Whenever detailed properties are known for the high redshift submm detected sources, which is the case for 2-3 objects, they have properties very similar to the local ULIRGs in terms of L_{FIR} , gas mass and star formation. If the submm detected objects are at high redshift they must have L_{FIR} exceeding $10^{12} L_{\odot}$, or they would not be detected with present day instrumentation. They are therefore likely to occupy the same region of the LT-relation as the local ULIRGs.

Making the assumption that the high redshift population as a whole is similar to the local ULIRGs, the local sample can be used as a template.

While the local sample shows a remarkably small dispersion in the shape of the long wavelength part of their SEDs, they differ considerably at mid-IR wavelengths. In this wavelength regime the IR emission is likely to show optical depth effects. The resulting SED is then dependent on the geometry of the emitting region and its orientation relative to the observer. The presence of an AGN would also be most apparent in this wavelength regime (see Klaas et al. 2001). While the shape of the SED at mid-IR contains substantial diagnostic power for the presence of a compact heating source for the dust, whether it is massive star formation or an AGN, it does not affect the use of submm bands for photometric redshifts as long as $z < 10$.

4.2. Comparison with other methods

The assumption made here of the existence of a template SED is exactly the same as done when using the radio-FIR spectral index method (Carilli & Yun 1999, 2000). The main difference between the two methods is that the FIR SED method does not need to exclude radio-loud AGNs, and it works out to redshifts $z \sim 5$. This is important since it is very difficult or impossible to distinguish between high redshift low-luminosity AGNs and non-AGNs among μJy radio continuum sources without milli-arcsecond imaging. One example of a high redshift radio-loud AGN, detected both as a submm source and in radio continuum is the gravitationally lensed H1413+117. The observed submm flux is much lower than expected from the radio continuum flux (Carilli & Yun 1999). The sample used here consists of a mixture of pure starburst and AGNs systems (Klaas et al. 2001); 8 are designated as starburst systems, 13 as LINERs, 8 as Seyferts (2 Sy 1 and 6 Sy 2), and 8 remain unassigned of a spectral class. As discussed above, the presence of an AGN is most evident in the mid-IR range and not at $\lambda > 60\mu\text{m}$.

An alternative photometric redshift method for use with FIR and submm observations was presented by Hughes et al. (2002). This method uses a large number of template SEDs, containing both starburst systems and AGNs, spanning a large range of intrinsic luminosities. The local IRAS $60\mu\text{m}$ luminosity function is evolved with redshift to explain the observed number-counts. The luminosity function is then randomly populated by the SEDs from the template catalog. Photometric redshifts are determined by calculating the probability that the colors of an observed submm source are consistent with the colors of every template SED at a given redshift. No correlation between the SED, luminosity and redshift is assumed. While models of this kind incorporate lower luminosity objects, the existing instrumentation

limits detection of high redshift objects to the most luminous ones. Until submm observations can routinely be done with rms noise levels of 0.1 mJy or lower, and in view of a possible luminosity-temperature relation, it seems prudent to restrict the template to objects with luminosities large enough to be detectable at high redshifts.

4.3. Comparison with observations

The flux density ratio $450\mu\text{m}/850\mu\text{m}$, derived from the template, as a function of redshift is shown in Fig. 8. Also shown are measured flux density ratios for high- z sources with known spectroscopic redshifts (see Table 2). Six of these are taken from a survey of gravitationally lensed AGNs (Barvainis & Ivison 2002). Three are submm detected galaxies with known redshift: SMM02399-0136 at $z = 2.81$ (Ivison et al. 1998), SMM02399-0134 at $z = 1.06$ and SMM1411+0252 at $z = 2.56$ (Ivison et al. 2000). Two sources detected by ISO at $170\mu\text{m}$ (Chapman et al. 2002): FN1-40 at $z = 0.45$ and FN1-64 at $z = 0.91$. Two additional gravitational lenses are also included, F10214+4724 at $z = 2.3$ (Rowan-Robinson et al. 1993) and APM08279+5255 at $z = 3.91$ (Irwin et al. 1998). The ISO sources are situated at relatively small redshifts and still have large uncertainties associated with their observed $450\mu\text{m}$ flux densities. Their predicted redshifts with the present photometric method are therefore uncertain. Nevertheless, the present method achieves a better result than the radio-FIR method which predicts redshifts of 1.1 and 1.3 instead of the spectroscopically derived 0.45 and 0.9.

Most of the sources shown in Fig. 8 and listed in Table 2 are gravitationally lensed and it is possible that differential magnification can distort the flux density ratios. This can happen if the emission regions dominating at $450\mu\text{m}$ has a smaller spatial extent than that of $850\mu\text{m}$. The effect would be to enhance the $450\mu\text{m}$ flux relative to that at $850\mu\text{m}$ and move the data points upwards in the diagram. This, however, is only expected to be of concern for the most strongly lensed sources. Indeed, the data points deviating significantly from the expected ratios are due to the strongest lenses (F10214+4724 and APM08279+5255). Another deviant source is SMM J02399-0134 with a spectroscopic redshift of $z = 1.06$, where the indicated photometric redshift is $2.2_{-0.6}^{+0.9}$ (see Table 2). This, however, is a redshift where the present method is less accurate due to the relatively small redshift. Apart from these three sources, the agreement with the redshift expected from the template model is good.

The low redshift sample of Dunne et al. (2001) generally fall below the predicted flux density ratio (given their redshift). This sample, however, only contains two sources which can be classified as ULIRG and hence, is not expected to conform to the ULIRG template. In particular, their average dust temperature is considerably lower (Dunne et al. 2001), in

agreement with a possible luminosity-temperature relation.

The spectroscopic and photometric redshifts are given in Table 2. The photometric redshifts are given with the errors calculated as a convolution of the photometric uncertainty and the 95% confidence limit derived from the template SED. The spectroscopic and photometric redshifts are compared graphically in Fig. 9. The uncertainty is dominated by the errors associated with the $450\mu\text{m}$ flux densities rather than the spread in template flux ratios.

4.4. Photometric to spectroscopic redshifts

Ultimately it is preferable to determine the redshift of all the submm detected galaxies spectroscopically. As mentioned in Sect. 1 this is in most cases very difficult due to the very weak emission at optical and NIR wavelengths. An alternative method will become available when ALMA (Atacama Large Millimeter Array) comes on-line. The sensitivity of this interferometer will be high enough to allow detection of CO emission from high redshift objects in a relatively short observing time (Blain et al. 2000). The instantaneous wavelength coverage will be much larger than present day instruments. The projected bandwidth is 16 GHz, corresponding to a redshift interval $\Delta z/z \approx 0.2 - 0.3$ in the 3mm atmospheric window. Although still relatively limited, it represents an order of magnitude improvement to existing millimeter and submillimeter instruments. The 3mm atmospheric window is ideal for searching for high redshift CO emission. Except for a redshift interval $0.44 \leq z \leq 1.0$, there will always be at least one CO rotational transition within 80 – 115 GHz. For redshift $z > 3$ there will be at least two transitions within the band.

If the photometric errors can be reduced to such a level that the uncertainty in the photometric redshift is dominated by the dispersion in template SED, the redshift uncertainty would be $\sim 30\%$ for redshifts $z > 1.5$. This is illustrated in Fig. 10, where $\Delta z/z$ is plotted as a function of redshift for the 95% and 90% confidence limit of the template SED. Also shown in Fig. 10 are the corresponding $\Delta z/z$ values of four CO transitions as observed in the 3mm band with the projected ALMA receiver bandwidth of 16 GHz. The 3mm band used here stretches from 80 GHz to 116 GHz, although the first receiver implementation is likely to cover a somewhat smaller band. Using higher frequencies results in a smaller redshift coverage and does not cover the rotational transitions believed to give the strongest signal (e.g. Combes, Maoli & Omont 1999). For the highest redshifts covered by the 3mm band, and thus the higher J-transitions, the redshift uncertainty in the photometric method is comparable or smaller than the redshift coverage of the ALMA bandwidth. For lower redshifts it will be necessary to use two tunings in order to bracket a photometrically

estimated redshift. Improvements of the photometric redshift method may remedy this, making it possible to use a single tuning of ALMA when searching for redshifted CO emission even for lower redshift sources.

5. Conclusion

Despite a serious degeneracy between the dust temperature and the redshift for a modified blackbody curve, it is shown that an average dust spectral energy distribution, based on a local sample of ultraluminous IR galaxies, can be used for photometric redshift determination in the interval $1 < z < 5$.

The local sample of ultraluminous IR galaxies (Klaas et al. 2001) shows a remarkably small dispersion in the shape of the SED at wavelengths longward of $\lambda = 50\mu\text{m}$. The local sample contains both starburst and AGN dominated sources.

Using this template and the internal dispersion in its shape, it is shown that observations at two fixed submm wavelengths, e.g. $450\mu\text{m}$ and $850\mu\text{m}$, can be used to determine the photometric redshift of galaxies in the redshift range $1 < z < 5$. The uncertainty in the redshift arising from the template SED amounts to $\Delta z/z \sim 0.3$, with an improvement at the highest redshift range.

Acknowledgement Careful reading and valuable comments from Duilia de Mello is gratefully acknowledged. Thanks to the referee U. Klaas for careful reading of the manuscript and suggestions which improved the presentation of the paper.

REFERENCES

- Barger, A. J., Cowies, L. L., Sanders, D. B., Fulton, E., Taniguchi, Y., et al. 1998, *Nature*, 394, 248
- Barvainis, R. and Ivison, R. 2002, *ApJ*, in press (astro-ph/0201424)
- Blain, A. W., 1999, *MNRAS*, 309, 955
- Blain, A. W., Frayer, D. T., Bock J. J. and Scoville, N. Z. 2000, *MNRAS*, 313, 559
- Blain, A. W., Barnard, V. E. and Chapman S. C. 2002, *MNRAS*, in press, (astro-ph/0209450)
- Carilli, C. L. and Yun, M. S. 1999, *ApJ*, 513, L13

- Carilli, C. L. and Yun, M. S. 2000, *ApJ*, 530, 618
- Chapman, S. C., Smail, I., Ivison, R. J., Helou, G., Dale, D. A., Lagache, G. 2002a, *ApJ*, 573, 66
- Chapman, S. C., Barger, A. J., Cowie, L. L., Scott, D., Borys, C., et al. 2002b, *ApJ*, in press, (astro-ph/0211075)
- Cimatti, A., Andreani, P., Röttgering, H. and Tilanus, R. 1998, *Nature*, 392, 895
- Combes, F., Maoli, R. and Omont A. 1999, *A&A*, 345, 369
- Condon, J. J., 1992, *ARA&A*, 30, 575
- Devriendt, J. E. G. and Guiderdoni, B. 2000, *A&A*, 363, 851
- Downes, D. and Solomon P. M. 1998, *ApJ*, 507, 615
- Dunne, L., Eales, S., Edmunds, M., Ivison, R. Alexander, P. and Clements, D. L. 2000, *MNRAS*, 315, 115
- Dunne, L. and Eales, S. A. 2001, *MNRAS*, 327, 697
- Dunne, L., Clements, D. L. and Eales, S. A. 2001, *MNRAS*, 319, 813
- Eales, S., Lilly, S., Gear, W., Dunne, L., Bond, J. R., et al. 1999, *ApJ*, 515, 615
- Efstathiou, A., Rowan-Robinson, M. and Siebenmorgen R. 2000, *MNRAS*, 313, 734
- Fixsen, D. J., Dwek, E., Mather, J. C., Bennett, C. L. and Shafer R. A. 1998, *ApJ*, 508, 123
- Fox, M. J., Efstathiou, A., Rowan-Robinson, M., Dunlop, J. S., Scott, S., et al. 2002, *MNRAS*, 331, 839
- Frayser, D. T., Ivison, R. J., Scoville, N. Z., Yun, M., Evans, A. S., et al. 1998, *ApJ*, 506, L7
- Frayser, D. T., Ivison, R. J., Scoville, N. Z., Evans, A. S., Yun, M. S., et al. 1999, *ApJ*, 514, L13
- Gispert, R., Lagache, G., and Puget J.-L. 2000, *A&A*, 360, 1
- Granato, G. L., Danese, L. and Franceschini, A. 1996, *ApJ*, 460, L11
- Guiderdoni, B., Hivon, E., Bouchet F. R. and Maffei, B. 1998, *MNRAS*, 295, 877
- Hildebrand, R. H. 1983, *QJRAS*, 24, 267

- Hughes, D. H., Dunlop, J. S. and Rawlins, S. 1997, MNRAS, 289, 766
- Hughes, D. H., Serjeant, S., Dunlop, J., Rowan-Robinson, M., Blain, A., et al. 1998, Nature, 394, 241
- Hughes, D. H., Aretxaga, I., Chapin, E. L., Gaztanaga, E., Dunlop, J. S., et al. 2002, MNRAS in press (astro-ph/0111547)
- Irwin M. J., Ibata, R. A., Lewis, G. F., and Totten, E. J. 1998, ApJ, 505, 529
- Iverson, R. J., Smail, I., Le Borgne, J.-F., Blain, A. W., Kneib, J.-P., et al. 1998, MNRAS, 298, 583
- Iverson, R. J., Smail, I., Barger, A. J., Kneib, J.-P., Blain, A. W., et al. 2000, MNRAS, 315, 209
- Kaviani, A., Haehnelt, M. G., and Kauffmann, G. 2002, MNRAS, in press, (astro-ph/0207238)
- Klaas, U., Haas, M., Müller, S. A. H., et al., 2001, A&A, 379, 823
- Lewis, G. F., Chapman, S. C., Ibata, R. A., Irwin, M. J. and Totten, E. J. 1998, ApJ, 505, L1
- Lutz, D., Dunlop, J. S., Almaini, O., Andreani, P., Blain, A., et al. 2001, A&A, 378, 70
- Nyman, L.-Å., Lerner, M., Nielbock, M., Anciaux, M., Brooks, K., Chini, R., et al. 2001, ESO Msngr, 106, 40
- Puget J.-L., Abergel, A., Bernard, J.-P., Boulanger F., Burton, W. B., Désert, F.-X. and Hartmann D. 1996, A&A, 308, L5
- Rigopoulou, D., Spoon, H. W. W., Genzel, R., et al. 1999, AJ, 118, 2625
- Rowan-Robinson, M. 1986, MNRAS, 219, 737
- Rowan-Robinson, M. 1992, MNRAS, 258, 787
- Rowan-Robinson, M., Efstathiou, A., Lawrence, A. Oliver, A., Taylor, A., et al. 1993, MNRAS, 261, 513
- Sanders, D. B. and Mirabel I. F. 1996, ARA&A, 34, 749
- Scott, S. E., Fox, M. J., Dunlop, J. S., Serjeant, S., Peacock, J. A., et al., 2002, MNRAS, 331, 817

Smail, I., Ivison, R. and Blain A. 1997, ApJ, 490, L5

Smail, I., Ivison, R. J., Owen, F. N., Blain, A. W. and Kneib, J.-P. 2000, ApJ, 528, 612

Smail, I., Ivison, R. J., Blain, A. W. and Kneib, J.-P., 2002, MNRAS, 331, 495

Wiklind, T. and Alloin, D. 2003, Dark Matter and Gravitational Lensing, eds. F. Courbin,
D. Minniti, Springer-Verlag

Yun, M. S. and Carilli, C. L. 2002, ApJ, 568, 88

Table 1. SIMBA data at $1250\mu\text{m}$

Name	S_{1250} mJy	σ mJy	Comments
00199-7426	49	13	
05189-2524	11	3	
06035-7102	<43	–	3σ
06206-6315	<13	–	3σ
17208-0014	64	13	
20100-4156	21	6	
E148IG002	<16	–	3σ
23230-6726	<21	–	3σ

Note. — Sources from the Klaas et al. (2001) sample observed with the SIMBA bolometer array at the SEST in October 2002.

Table 2. Submm flux data

Name	z_{spec}	f_{850} (mJy)	σ_{850} (mJy)	f_{450} (mJy)	σ_{450} (mJy)	R^a	z_{phot}	Reference
SMM J14011+0252	2.56	12.3	1.7	42	7	3.4 ± 0.7	$2.4_{-0.5}^{+0.7}$	(1) (2)
SMM J02399-0136	2.81	23.0	1.9	85	10	3.7 ± 0.5	$2.2_{-0.3}^{+0.4}$	(1) (2)
HR10	1.44	8.7	1.6	<180		<21	–	(3)
SMM J02399-0134	1.06	11.0	1.9	42	10	3.8 ± 1.1	$2.2_{-0.6}^{+0.9}$	(1)
FN1-64	0.91	5.9	1.4	50	19	8.5 ± 4.0	$0.2_{-}^{+1.6}$	(4)
FN1-40	0.45	6.3	1.4	42	30	6.7 ± 5.0	$0.8_{-}^{+3.7}$	(4)
SMM J09429+4658	–	17.2	1.9	61	7	3.5 ± 0.6	$2.3_{-0.4}^{+0.4}$	(1)
SMM J14009+0252	–	15.6	1.9	33	9	2.1 ± 0.6	$3.8_{-0.8}^{+1.1}$	(1)
SMM J00266+1708	–	18.6	2.4	<60		<3.2	> 2.6	(5)
Lockman850.1	–	10.5	1.6	35	10	3.3 ± 1.1	$2.5_{-0.7}^{+1.1}$	(6)
HDF850.1	–	7.0	0.4	<21		<3.0	> 2.8	(7)
2237+0305	1.70	2.8	0.9	<17		<6.1	> 1.0	(8)
HE0230-2130	2.16	21.0	1.7	77	13	3.7 ± 0.7	$2.2_{-0.4}^{+0.5}$	(8)
F10214+4724	2.29	50.0	5.0	273	45	5.5 ± 1.1	$1.3_{-0.4}^{+0.5}$	(8)
H1413+117	2.56	58.8	8.1	224	38	3.8 ± 0.8	$2.2_{-0.5}^{+0.6}$	(8)
MG J0414+0534	2.64	25.3	1.8	66	16	2.6 ± 0.7	$3.2_{-0.6}^{+1.0}$	(8)
UM673	2.73	12.0	2.2	<40		<3.3	> 2.5	(8)
RX J0911.4+0551	2.81	26.7	1.4	65	19	2.4 ± 0.7	$3.4_{-0.7}^{+1.2}$	(8)
MG J0751+2716	3.21	25.8	1.3	71	15	2.8 ± 0.6	$3.0_{-0.5}^{+0.8}$	(8)
CLASS B1359+154	3.24	11.5	1.9	39	10	3.4 ± 1.0	$2.4_{-0.7}^{+1.0}$	(8)
APM08279+5255	3.91	84.0	3.0	285	11	3.4 ± 0.2	$2.4_{-0.2}^{+0.2}$	(8)

$$^a R = S(450\mu\text{m})/S(850\mu\text{m})$$

Note. — References: (1) Smail et al. (2002) (2) Ivison et al. (2000); (3) Cimatti et al. (1998); (4) Chapman et al. (2002); (5) Frayer et al. (2000); (6) Lutz et al. (2001); (7) Hughes et al. (1998); (8) Barvainis & Ivison (2002)

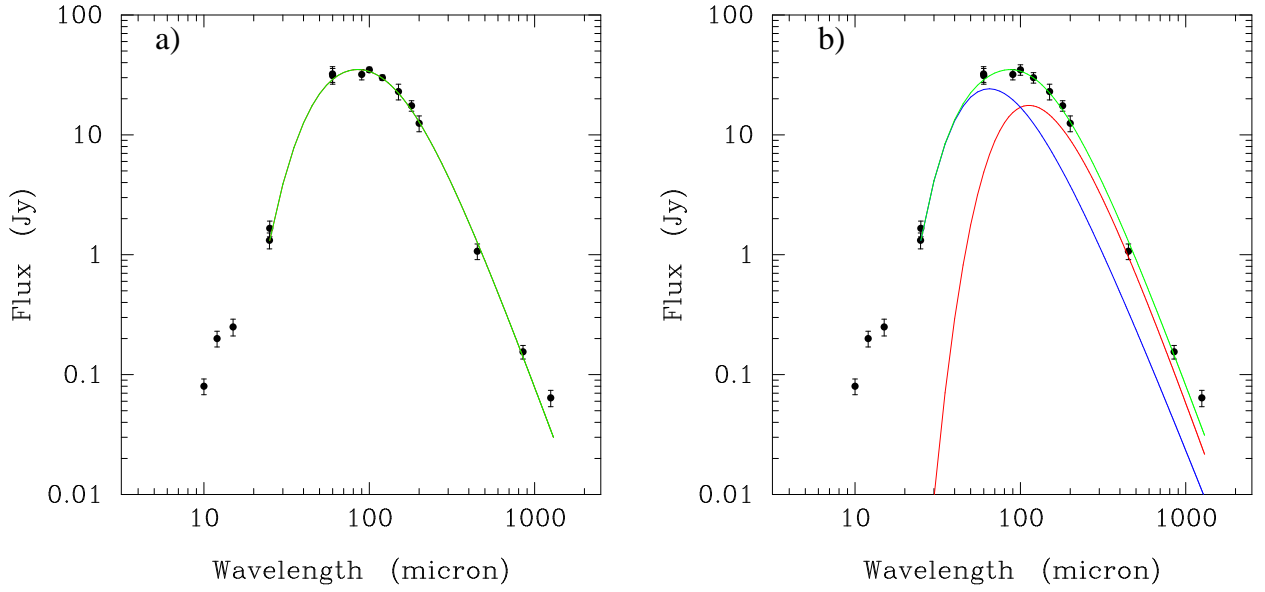


Fig. 1.— **a)** Fit of a one-component modified blackbody function to the observed flux densities of the local ULIRG 17208–0014. The parameters for the fit are: $\Omega = (9.1 \pm 1.1) \times 10^{-14}$, $\beta = 1.8 \pm 0.2$, $\nu_0 = (1.4 \pm 0.2) \times 10^{12}$ Hz, $T_d = 59 \pm 1.4$ K. **b)** Fit of a two-component modified blackbody function to the same flux density values. The fit is as good as the one-component and results in the following values: $\Omega = 34.4 \times 10^{-14}$, $\beta = 1.6$, $\nu_0 = 8.6 \times 10^{12}$ Hz, $T_d = 53$ K, for the warm component, and $\Omega = 371 \times 10^{-14}$, $\beta = 2.0$, $\nu_0 = 5.9 \times 10^{12}$ Hz, $T_d = 27$ K, for the cold component.

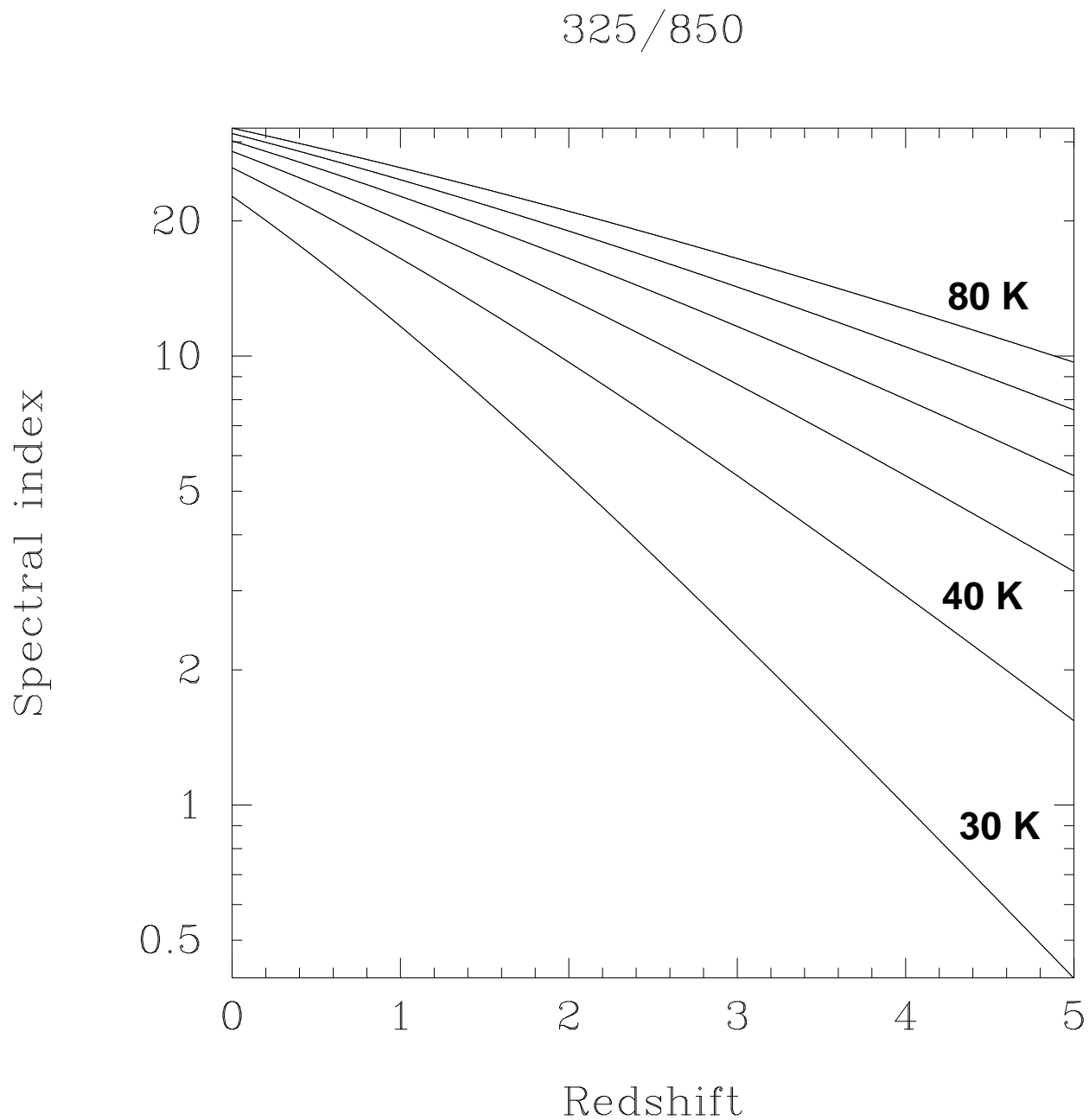


Fig. 2.— The flux ratio at fixed observed wavelengths $325\mu\text{m}/850\mu\text{m}$ for a modified blackbody spectral energy distribution as a function of redshift of the source. The flux ratios for 6 different dust temperatures are shown, illustrating the degeneracy between redshift and dust temperature for a given flux density ratio. The dust SED is represented by: $f_\nu \propto \nu^\beta B_\nu(T_d)$, where $\beta = 1.8$.

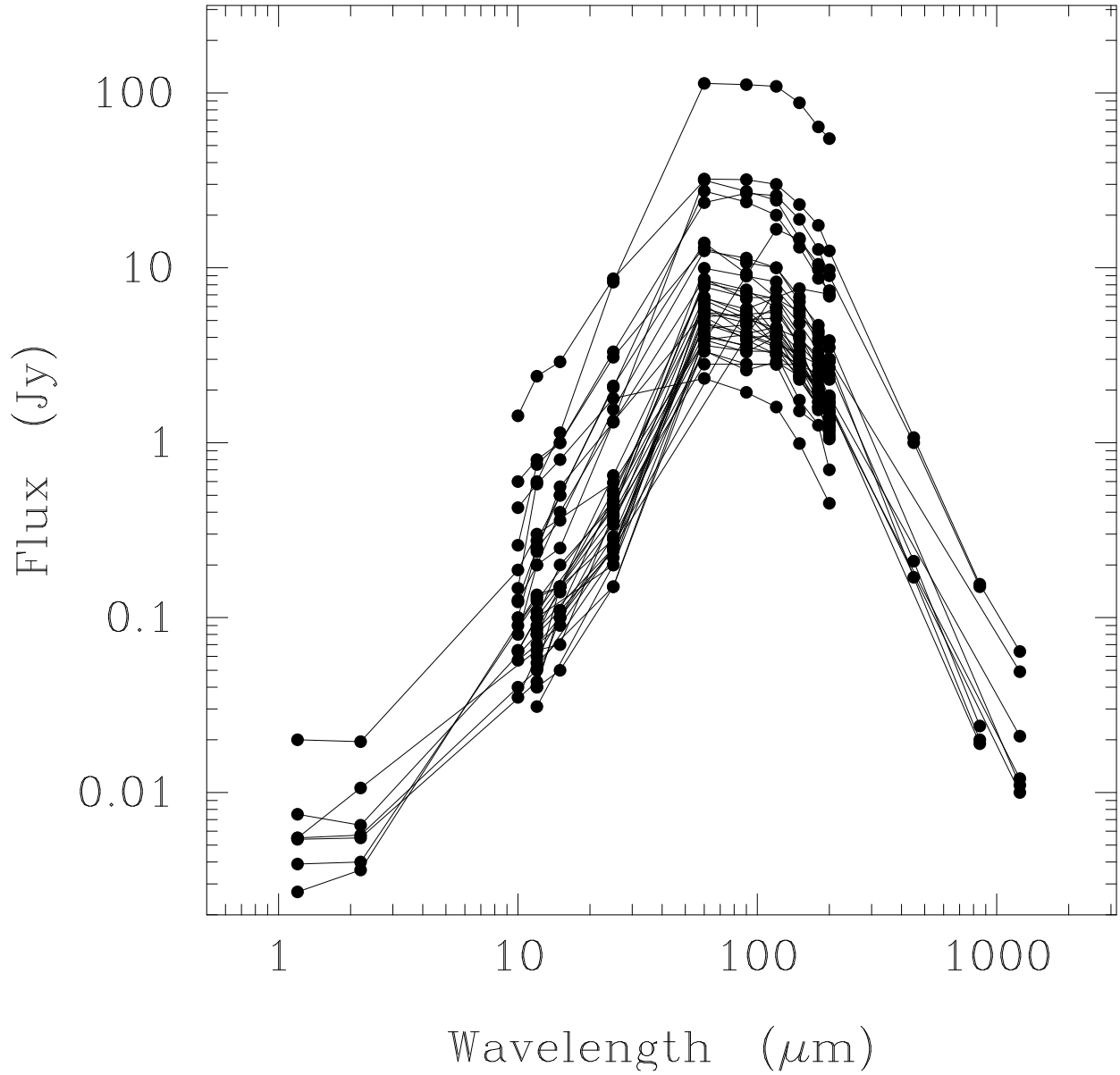


Fig. 3.— The spectral energy distributions of the 37 ULIRGs part of the local sample (from Klaas et al. 2001). The observed fluxes are plotted without any corrections or normalization. Despite a range of fluxes over two orders of magnitude, the general shape of the SEDs remains the same.

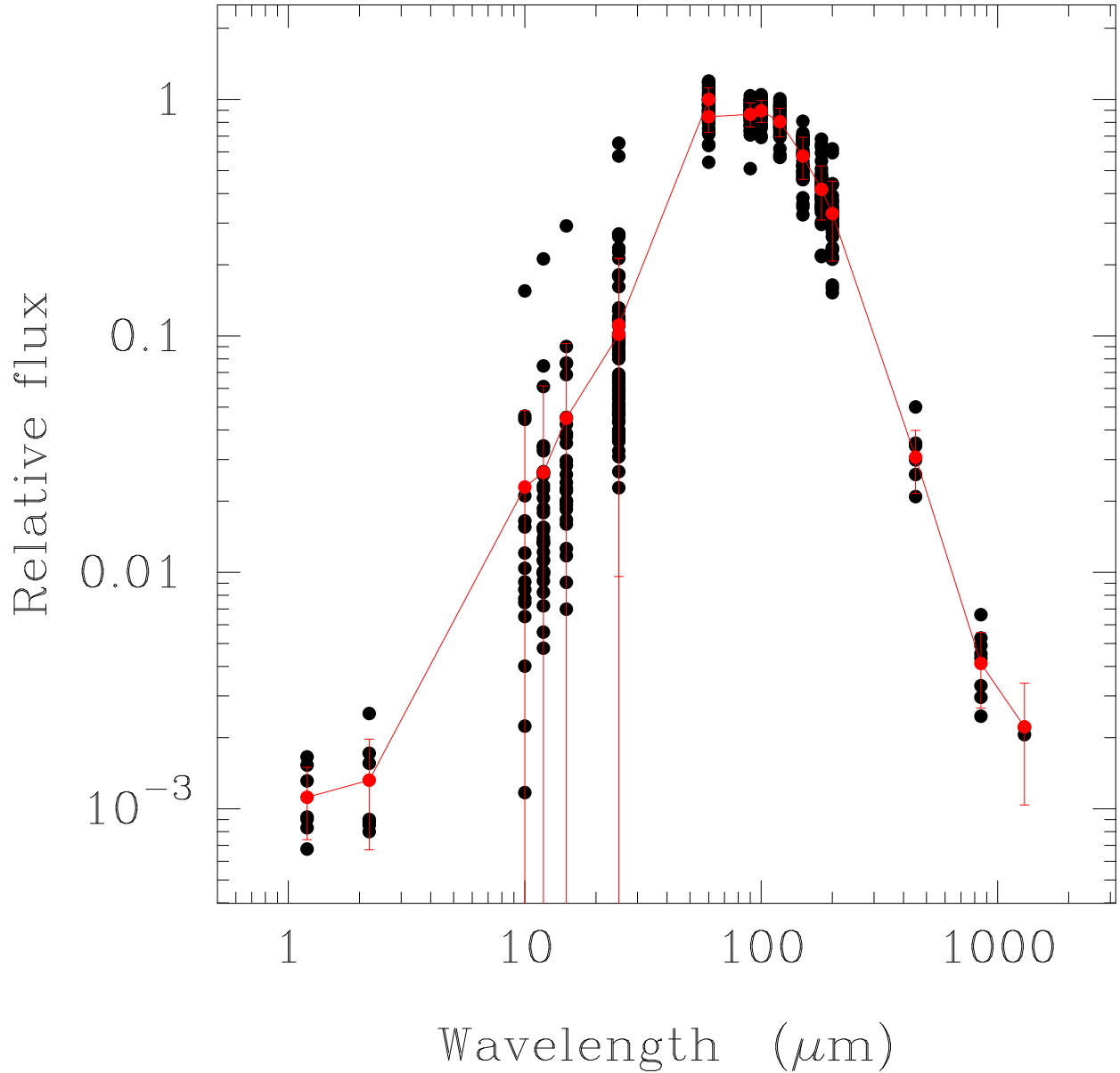


Fig. 4.— The spectral energy distributions of the 37 ULIRGs part of the local sample (from Klaas et al. 2001). Here the individual SEDs have been multiplied by a constant factor, chosen such that the overall dispersion is minimized. The individual data points, the average as well as the 1σ dispersions are shown (light grey). The line just connects the average flux measurement at each observed wavelength.

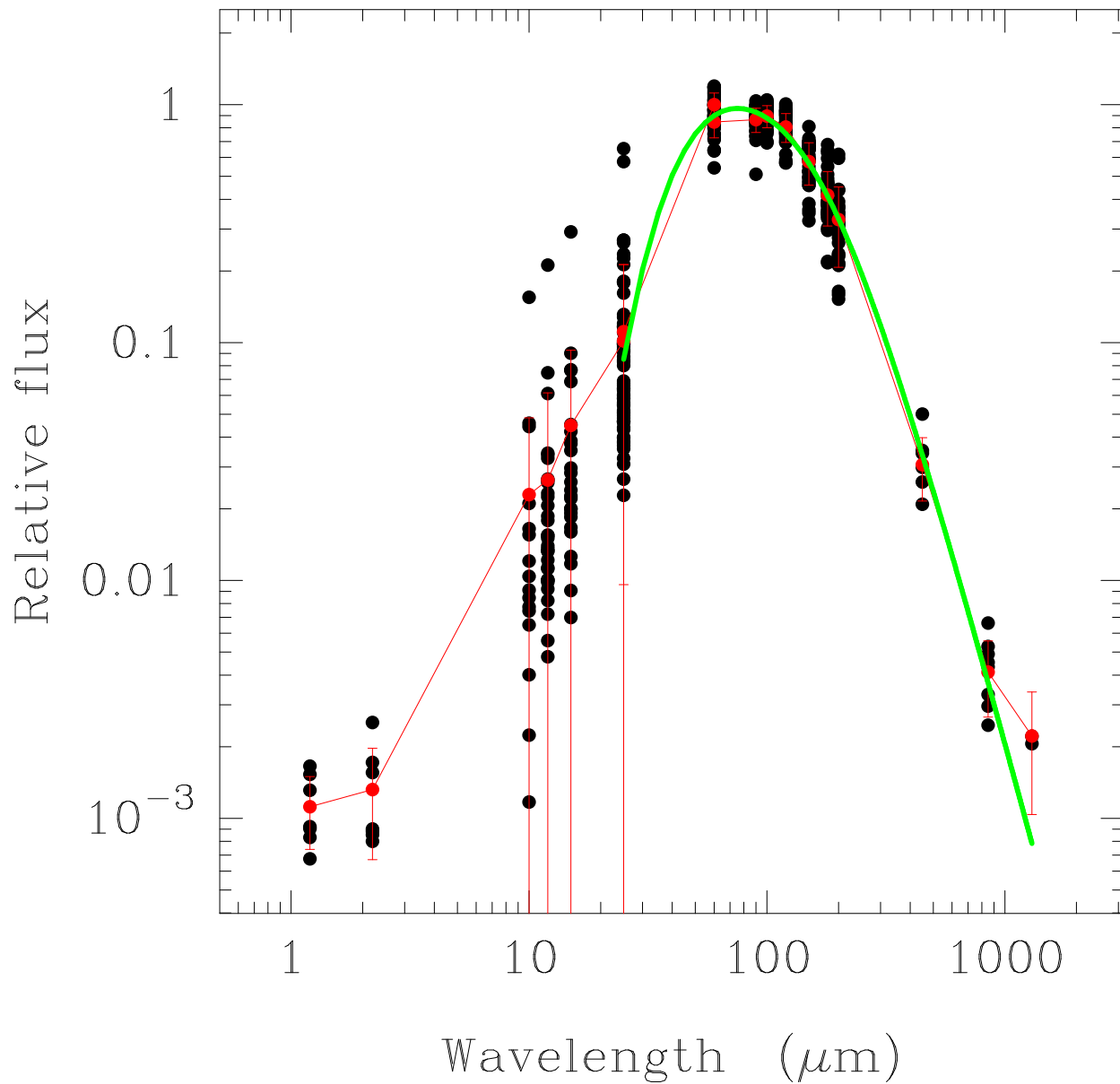


Fig. 5.— A fit of a modified blackbody curve (see Eq. 1) made to the average SED obtained by minimizing the overall dispersion. The fit has been made over the wavelength interval 60-850 μm . The best-fit parameters are: $\Omega = (1.6 \pm 0.6) \times 10^{13}$, $\beta = 1.8 \pm 0.5$, $\nu_0 = (1.2 \pm 0.4) \times 10^{12}$ Hz and $T_d = 68 \pm 9$ K.

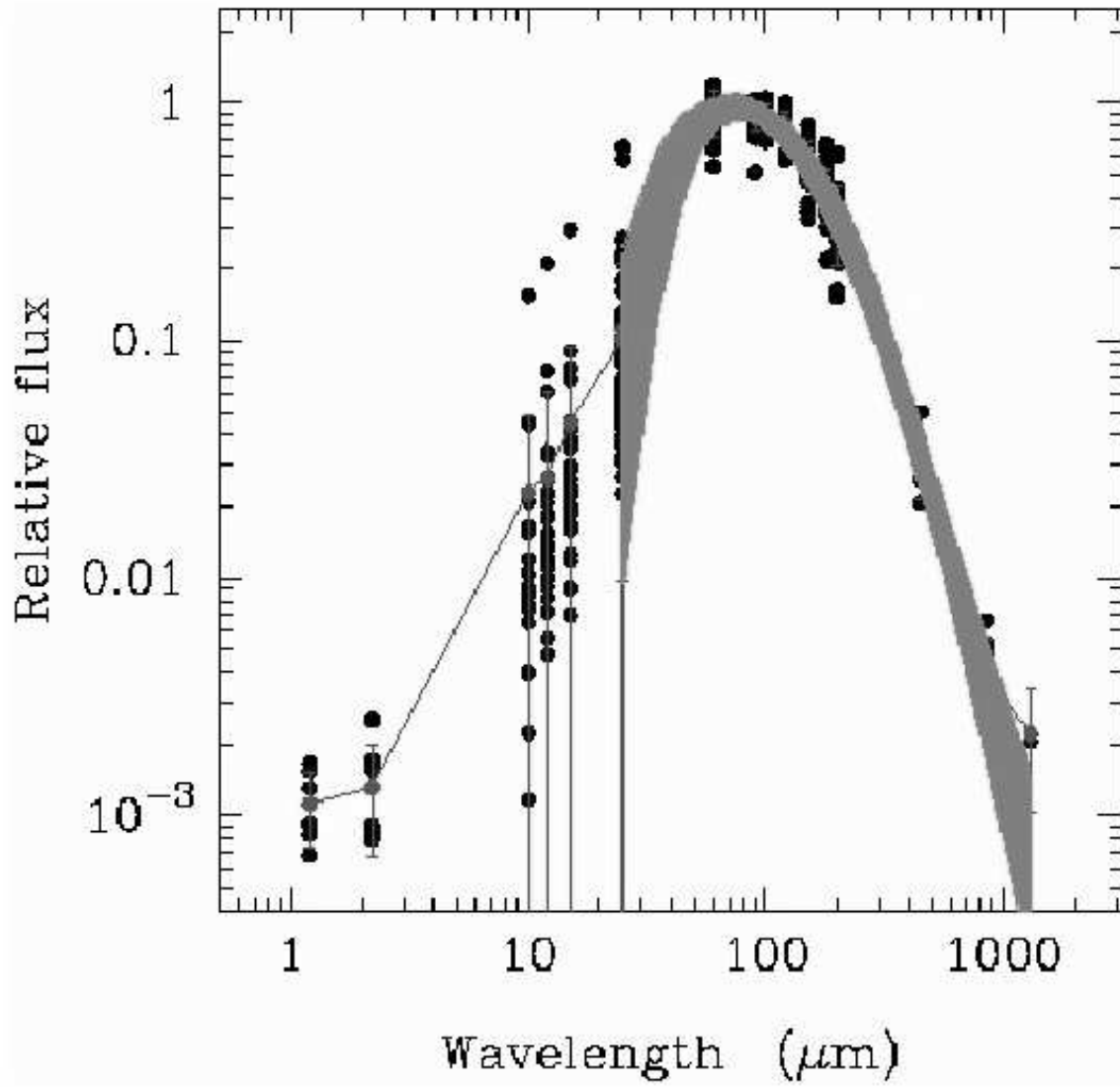


Fig. 6.— Fits of modified blackbody curves resulting from letting the flux density values at each wavelength vary uniformly $\pm 1\sigma$. The grey area represents 10^4 simulated fits.

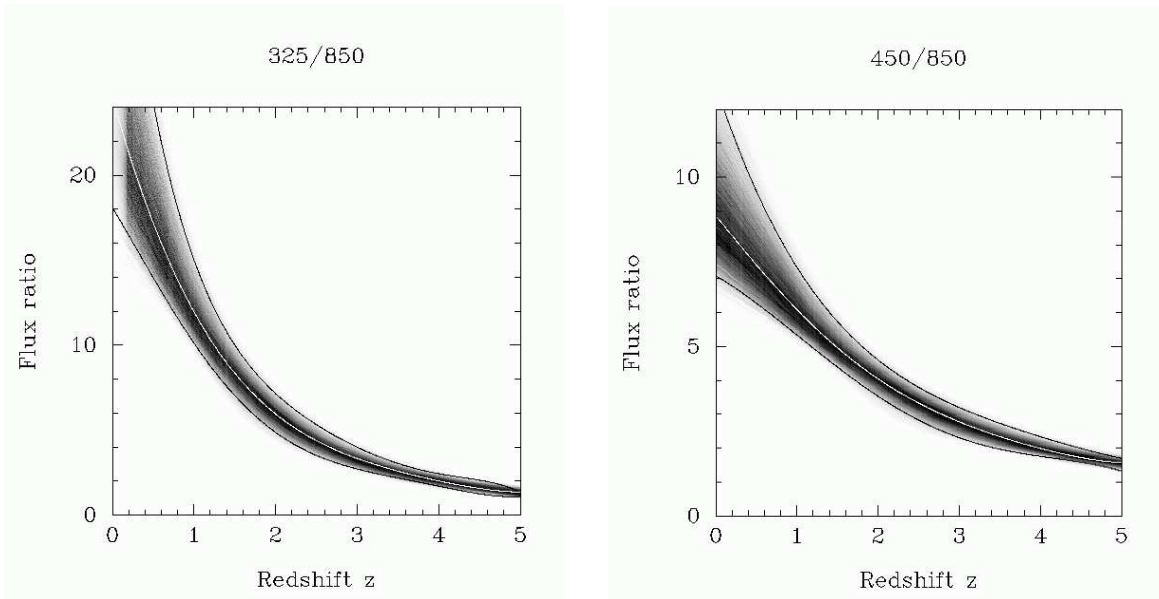


Fig. 7.— The ratio of two fixed wavelength bands, each of width 30 GHz, as a function of redshift of the emitting source. The grey area corresponds to the results from 10^4 Monte Carlo simulations and represents the density of curves passing through a given point (dark means high density). The maximum density is outlined by the white curve and it is flanked by two curves representing the boundary containing $\pm 95\%$ of the curves. **a)** The ratio of $325\mu\text{m}/850\mu\text{m}$ and **b)** $450\mu\text{m}/850\mu\text{m}$. The $450\mu\text{m}$ and $850\mu\text{m}$ bands are chosen to represent the existing SCUBA filters.

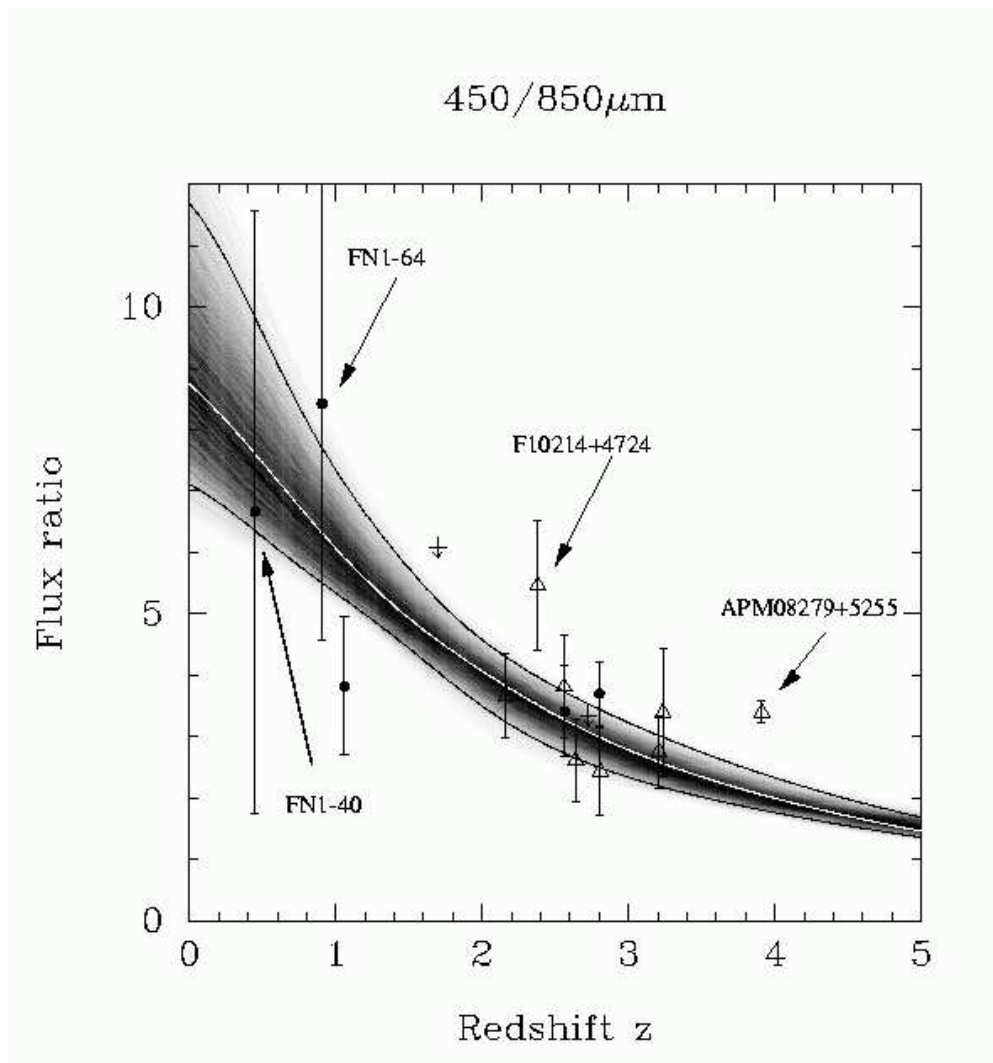


Fig. 8.— The flux ratio of $450\mu\text{m}/850\mu\text{m}$, measured at fixed wavelenghts, versus redshift of the emitting source. The results from 10^4 Monte Carlo simulations are shown. The greyscale represents the density of curves passing through a given point (dark means high density). The maximum density is outlined by the white curve and it is flanked by two curves representing the boundary containing $\pm 95\%$ of the curves. Also shown are the existing sources observed at both $450\mu\text{m}$ and $850\mu\text{m}$ and with known redshift. The open triangles are taken from a sample of high redshift QSOs (Barvainis & Ivison 2002). All of these are gravitationally lensed but differential magnification is likely to be significant only for the strongest lenses (IRAS F10214+4724 and APM08279+5255). Filled circles correspond to submm detected galaxies.

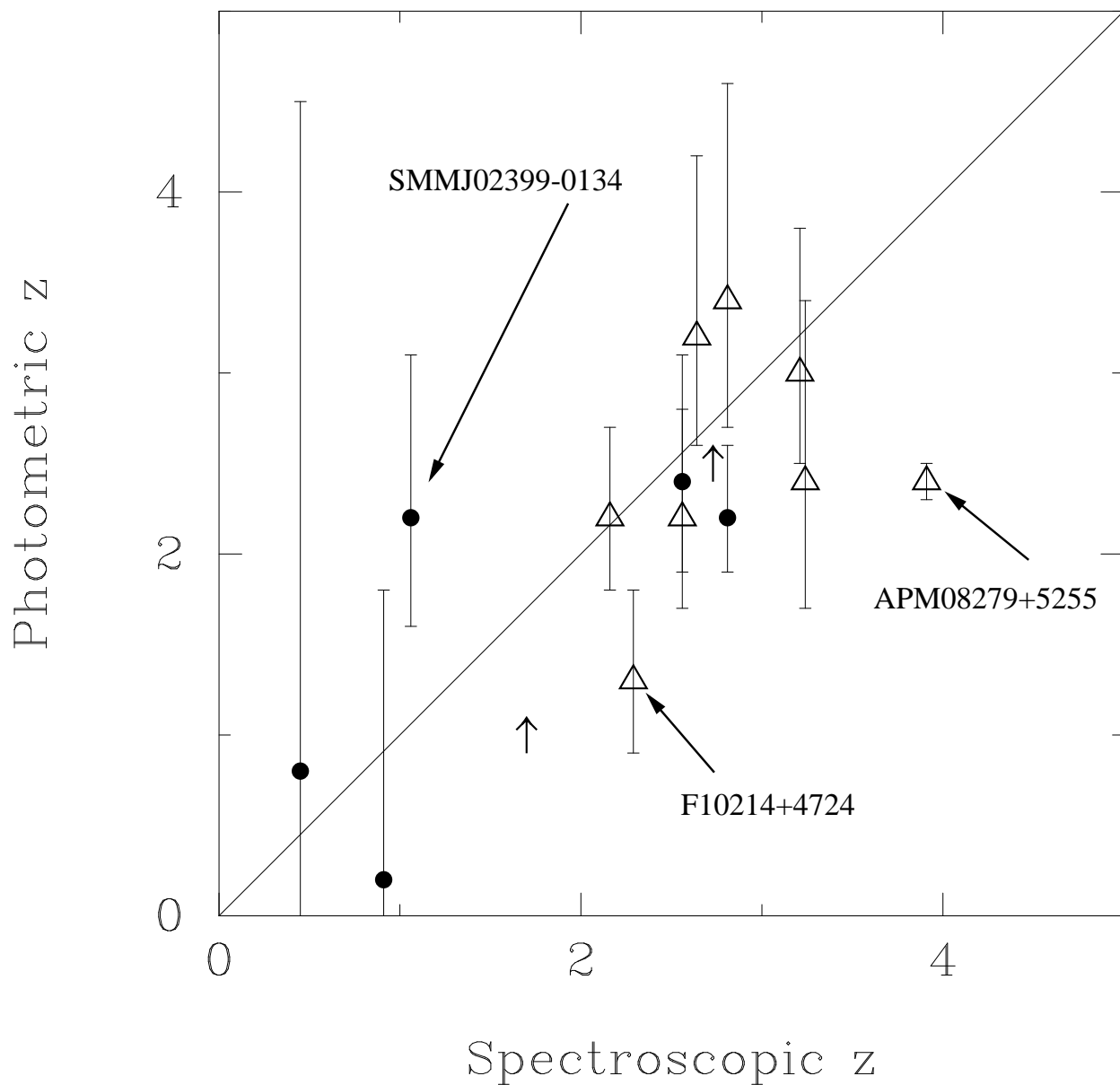


Fig. 9.— Comparison between photometric redshifts using the present method and spectroscopic redshift for a sample of submm detected objects and high- z quasars (see Table 2). The full drawn line corresponds to a one-to-one relation between photometric and spectroscopic redshifts and is not a fit to the data. The errors in photometric redshifts have been derived using the observed photometric errors convolved with the 95% confidence level for the template.

450/850 μm

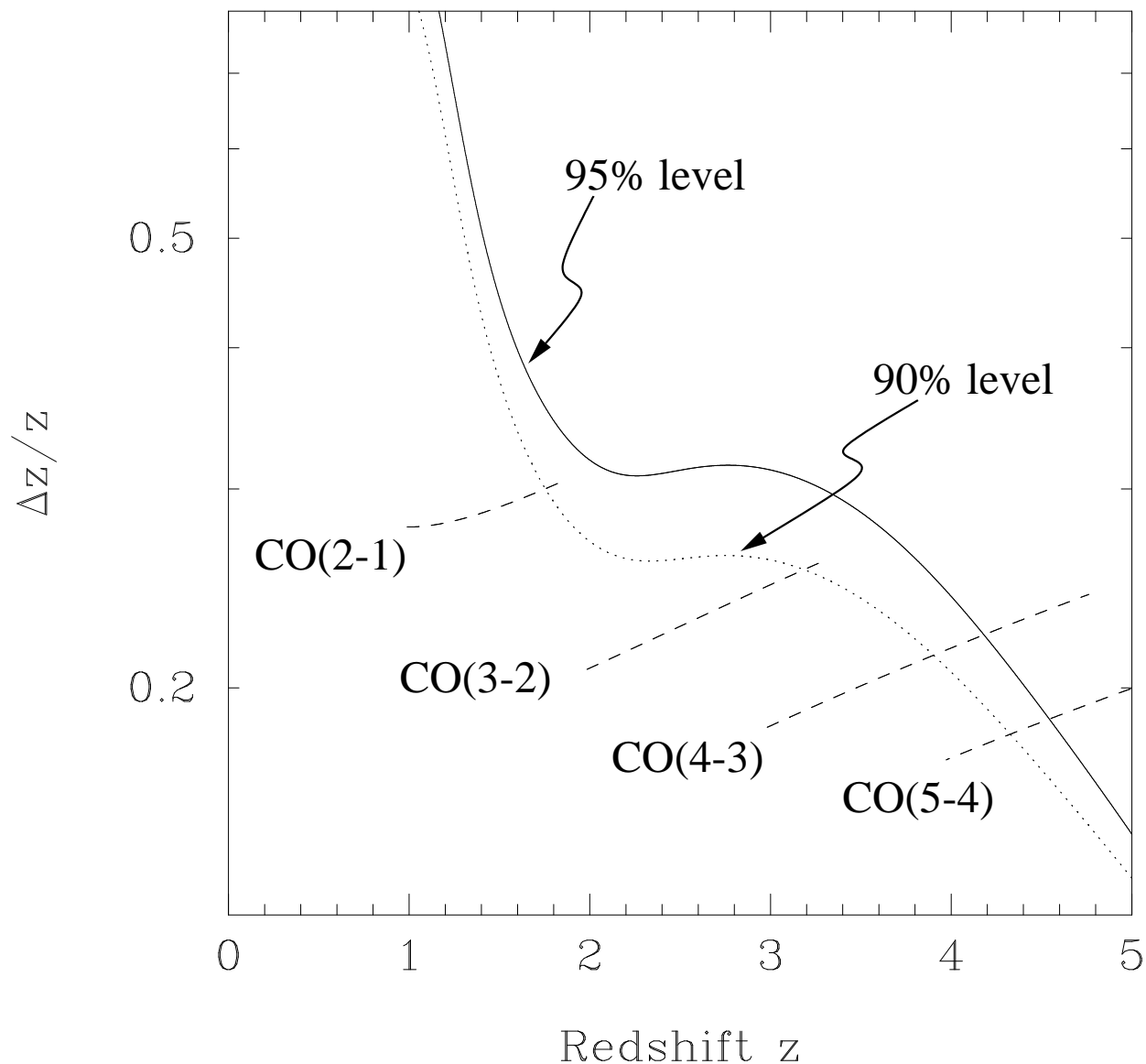


Fig. 10.— The uncertainty in redshift associated with the template, using the $\pm 95\%$ (full-drawn line) and $\pm 90\%$ (dotted line) confidence limits (the $\pm 95\%$ confidence limit is shown in Fig. 8). While $\Delta z/z$ is large for small redshifts, it drops to ~ 0.3 for $z > 1.5$ and even further at larger redshifts. Also shown is the $\Delta z/z$ coverage of 4 CO rotational lines with the planned ALMA receivers in the 3mm atmospheric windows. The redshift coverage depends on the observed frequency (the bandwidth being fixed at 16 GHz) and increases as a given transition is observed at higher redshift (lower observed frequency). Photometric redshifts are accurate enough to allow direct tuning for transitions at approximately $z > 3$.